Electrochemical Strain Dynamics in Noble Metal Nanocatalysts

Raphaël Chattot, Isaac Martens, Marta Mirolo, Michal Ronovsky, Florian
Russello, Helena Isern, Guillaume Braesch, Elisabeth Hornberger, Peter
Strasser, Eric Sibert, et al.

Electrochemical Strain Dynamics in Noble Metal Nanocatalysts

Raphaël Chattot [1,], Isaac Martens [1], Marta Mirolo [1], Michal Ronovsky [1], Florian Russello [1], Helena Isern Herrera [1], Guillaume Braesch [2], Elisabeth Hornberger [3], Peter Strasser [3], Eric Sibert [2], Marian Chatenet [2], Veijo Honkimäki [1], and Jakub Drnec [1]*

[1] European Synchrotron Radiation Facility, ID 31 Beamline, BP 220, F-38043 Grenoble, France

[2] Univ. Grenoble Alpes, Univ. Savoie Mont Blanc, CNRS, Grenoble INP*, LEPMI, 38000 Grenoble, France. *Institute of Engineering and Management Univ. Grenoble Alpes

[3] Electrochemical Energy, Catalysis and Material Science Laboratory, Department of Chemistry, Technische Universität Berlin, 10623 Berlin, Germany

*e-mail: (RC) raphael.chattot@grenoble-inp.org

ABSTRACT

The theoretical design of effective metal electrocatalysts for energy conversion and storage devices relies greatly on supposed unilateral effects of catalysts structure on electrocatalyzed reactions. Here, by using high-energy X-ray diffraction from the new Extremely Brilliant Source of the European Synchrotron Radiation Facility (ESRF-EBS) on device-relevant Pd and Pt nanocatalysts during cyclic voltammetry experiments in liquid electrolytes, we reveal the near ubiquitous feedback from various electrochemical processes on nanocatalyst strain. Beyond challenging and extending the current understanding of practical nanocatalysts behavior in electrochemical environment, the reported electrochemical strain provides experimental access to nanocatalysts absorption and adsorption trends (*i.e.* reactivity and stability descriptors) *operando*. The ease and power in monitoring such key catalyst properties at new and future beamlines is foreseen to provide a discovery platform toward the study of nanocatalysts encompassing a large variety of applications, from model environments to the device level.

INTRODUCTION

Surface science has driven the development of commercial nanocatalysts for energy conversion and storage applications, by establishing the electronic descriptors that rationalize or even predict the activity of metallic surfaces for numerous reactions in the frame of the Sabatier principle: the ability of the surface to bind adsorbates and the strength of the bonds define the reaction thermodynamics and kinetics [1–5]. This seminal knowledge has allowed tremendous improvements in electrocatalytic materials according to the 'catalysts-by-design' [6] approach, where catalytic performance is tailored by the surface crystallographic structure and chemical composition [7–9]. Tacitly, this approach relies on the supposed unilateral causal relationship between the fixed nanocatalyst structure and the electrocatalyzed reaction mechanism/kinetics. However, various opposite relations, *i.e.* the catalyst structure alteration by the (electro)chemical environment, exist. Among them, irreversible degradation processes has received a lot

of attention. In fact, even the most noble metal based catalysts, such as Platinum (Pt) or Palladium (Pd) are subject to corrosion over the long term in the harsh conditions of proton (or anion) exchange membrane fuel cell (PEMFC, AEMFC) cathode and proton (or anion) exchange membrane water electrolyzer (PEMWE, AEMWE) anode [10,11], thus compromising the lifetime of those systems. In these particular cases, the electrochemical adsorption trend of oxygenated species does not only define the catalyst activity [3] but also its stability against dissolution according to the place exchange mechanism [12]. In addition, reversible structural modifications can also be observed. For example, (electrochemical) absorption of hydrogen (H) into the bulk of Pd (nano)crystal is known to induce sharp Pd lattice expansion, in the form of a phase transition [13–16]. As a result, the strain in Pd is classically used as a direct quantitative descriptor of hydrogen absorbed (the H:Pd ratio) [17–20], from the established near linear relationship between these two entities [19]. Lastly, surface X-ray diffraction on single crystals revealed the impact of electrochemical surface adsorption process on crystal strain [21–24]. Compared to bulk absorption, surface adsorption produces a much subtler effect since the interplanar distances from only the 2 or 3 first monolayers were found to be impacted by various adsorbates. However, despite the extremely high surface-to-volume ratio of nanomaterials and the urgent need for experimental techniques able to monitor the electrochemical adsorption trends of practical catalytic materials during operation, in-depth investigation of nanocatalyst 'electrochemical strain' has never been performed.

In this contribution, we use the light from the new 4th generation Extremely Brilliant Source of the European Synchrotron Radiation Facility (ESRF-EBS, Grenoble, France) to investigate the structural evolution of device-relevant, carbon-supported Pd and Pt nanocatalysts during various cyclic voltammetry experiments in liquid electrolytes (acid and alkaline). The brilliance and high-energy of the employed X-rays reveal catalysts microstructural information with unprecedented combined quality and temporal resolution for *operando* measurements. The first discovery is that, contrary to the current knowledge, the strain in carbon-supported Pd (Pd/C) and Pt (Pt/C) nanoparticles is permanently affected by the electrochemical environment. The impact of both electrochemical bulk hydrogen absorption and surface

adsorption processes are then investigated separately on Pd and Pt, respectively. Analysis of our structural data provide new insights in the mechanism of electroabsorbed hydrogen-induced phase transition in the Pd-H system and reveal the adsorption trends of Pt. Subsequent comparison between Pd and Pt shows absorption and adsorption phenomena produce close but distinctive structural changes allowing their disentanglement from strain measurements. Finally, further insights on the atomistic origin of electrochemical strain are presented, and its potential implication in electrocatalysis is discussed. These new results extend our understanding of noble nanomaterials behavior in electrochemical environments and provide versatile experimental access to reactivity and stability descriptors of practical nanocatalysts, *operando*.

RESULTS AND DISCUSSION

Unveiling electrochemical strain dynamics in noble metal nanocatalysts during cyclic voltammetry experiments

Figure 1.a shows a typical wide-angle X-ray scattering (WAXS) dataset obtained during cyclic voltammetry of Pd/C nanoparticles in N_2-purged 0.1 M NaOH electrolyte at room temperature. When probed with sufficiently bright and energetic X-rays (here 2.10^{12} photons s^{-1} at 78 keV), the electrocatalytic thin films (1.45 mg_{metal} cm^{-2} or 25 μg_{metal} cm^{-2} for transmission or grazing incidence configurations, respectively) contained in 3-electrode flow cells (**Figure S1** in Supporting Information) produce very low-noise signals on the detector in short exposure time (below 300 ms), which can then be further reduced to high-quality diffraction patterns of high temporal resolution (below 400 ms). Analyzing the full patterns with the Rietveld refinement method allows tracking the microstructure of the nanoparticles composing the catalyst, *e.g.* crystal phase structure, lattice constant or coherent domain size from the WAXS reflections position, intensity and shape (**Figure 1.b**). Note that the as-extracted lattice

constant values are by definition an average over the coherence length of the phase. In addition, the scale factor (the Bragg peaks' area) relates to the quantity of unit cells from the crystals contributing to the diffraction pattern. Details on the model used for the Rietveld method are given in the Methods section and in Supporting Information.
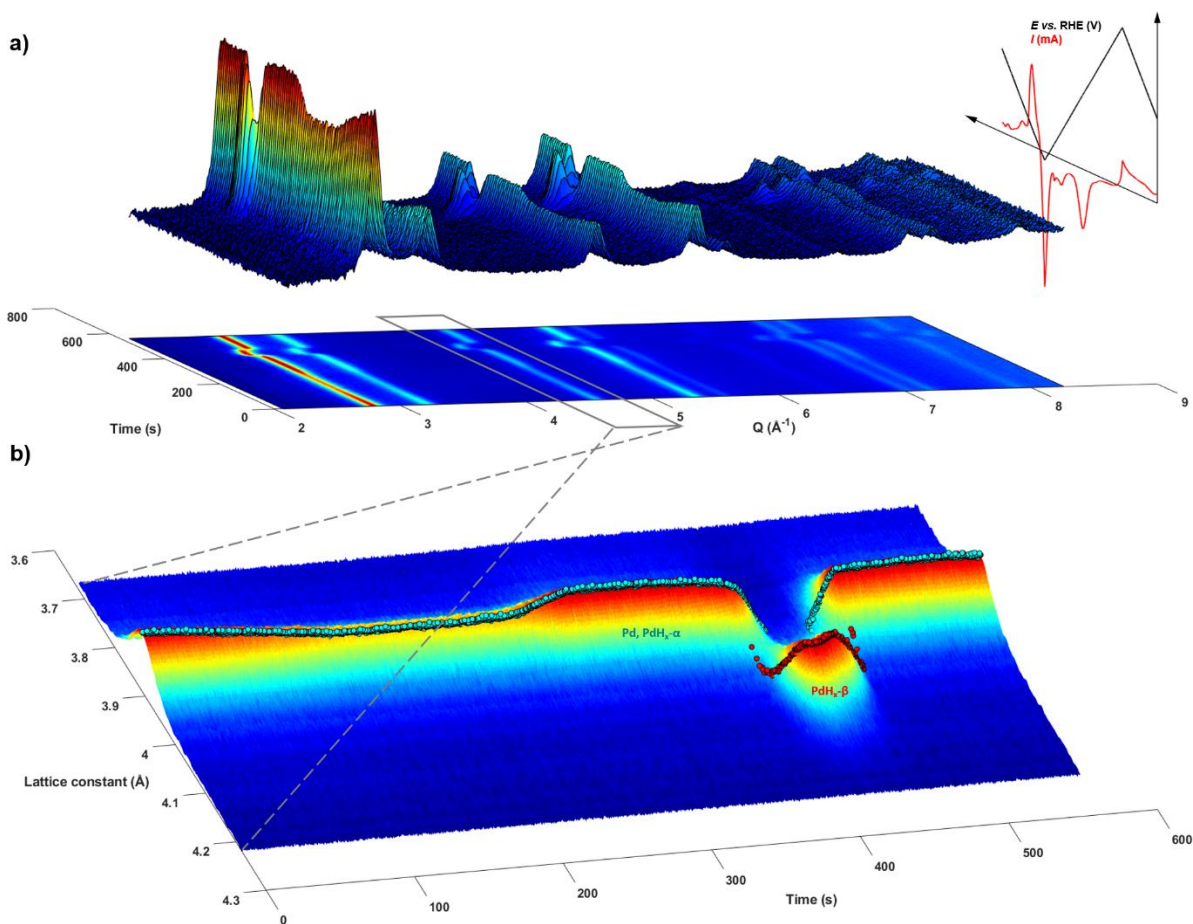
Figure 1. New light on Pd nanoparticles during cyclic voltammetry*. a) 3D representation and corresponding 2D projection of WAXS patterns intensities (1 over 20) plotted as a function of time and the momentum transfer Q recorded during Pd cyclic voltammetry experiment in N_2-purged 0.1 M NaOH electrolyte at room temperature. The evolutions of the electrochemical potential applied and measured electric current are also represented on the same time scale; b) surface plot focus on a narrow Q window showing the full time resolution evolution of the two phases (Pd, or PdH$_x$-α and PdH$_x$-β)[220] reflections. In b), the Q scale (left) is*

converted to the corresponding lattice constants, and the values calculated by Rietveld refinement of the full patterns are added on the top of the surface plot. The exposure time for WAXS measurement was 250 ms, leading to an overall temporal resolution of 333 ms. The electrode was loaded with 1.45 $mg_{metal}\ cm^{-2}$ and the potential sweep rate was 5 mV s^{-1}.

Cyclic voltammograms (**Figure 2.a** and **2b** for Pd/C and Pt/C, respectively) show the usual features of these noble metal electrodes, *e.g.* hydrogen evolution ($E < 0.05$ V *vs.* RHE), underpotential adsorption-absorption/desorption of hydrogen (H_{UPD}, $0.05 \leq E \leq 0.30$ V *vs.* RHE) and adsorption/desorption of oxygenated species ($E \geq 0.50$ V *vs.* RHE). Strikingly, the relative variations of the lattice constants and scale factors (in %, compared to their values measured in the double-layer region at $E = 0.5$ V *vs.* RHE), show near-permanent dependency with the electrode potential and history (**Figure 2.c** and **2d** for Pd/C and Pt/C, respectively). This suggests that the different electrochemical processes listed above produce important feedback, that we denote as 'electrochemical strain', on the catalysts microstructures. Electrode polarization at high potential ($E > 0.5$ V *vs.* RHE) leads to ~0.3% and 0.4% lattice constant expansion for Pd/C and Pt/C, respectively, accompanied with ~20% scale factor losses for the two materials. These changes are irreversible with the applied potential, as pronounced hysteresis are observed. For Pt, the trends agree with the pioneer work from Martens *et al.*, who used this indicator to investigate Pt oxidation dynamics [25]. Although quantitatively different, the trends for both Pd and Pt materials appear qualitatively similar at high potential. Electrode polarization at low potential ($E < 0.4$ V *vs.* RHE), however, leads to sharp differences in microstructural evolution. Only ~0.3% of maximum lattice expansion is observed for Pt *versus.* ~3.5% for Pd. These differences mainly originate from the well-known Pd's ability to absorb hydrogen compared to Pt. The PdH$_x$ $\alpha \leftrightarrow \beta$ phase transitions during cyclic voltammetry were clearly captured by the WAXS patterns (shifted set of reflections in **Figure 1**), and result in two distinct lattice constants and scale factors values (**Figure 2.c**). The Pd, or PdH$_x$-α phase corresponds to Pd when no or few hydrogen atoms are inserted in octahedral interstitial positions and PdH$_x$-β when larger number of hydrogen atoms are inserted in octahedral interstitial positions. The regions corresponding to the existence and co-existence of the different PdH$_x$ phases revealed by their scale factors are indicated in the

colored cyclic voltammogram (**Figure 2.a**). Whereas **Figure 2.d** reveals that adsorption and desorption of hydrogen produce rather potential-reversible variation of Pt lattice constant and preserve the nanoparticles coherence (constant and maximum scale factor), the phase transitions PdH_x $\alpha \leftrightarrow \beta$ appear irreversible with the potential. In the following, we will sequentially focus on the electrochemical strain from (i) the electrochemical hydrogen absorption on Pd and (ii) the hydrogen, anions and oxides adsorption on Pt, before discussing the complete picture of adsorption and/or absorption processes on both Pd and Pt.
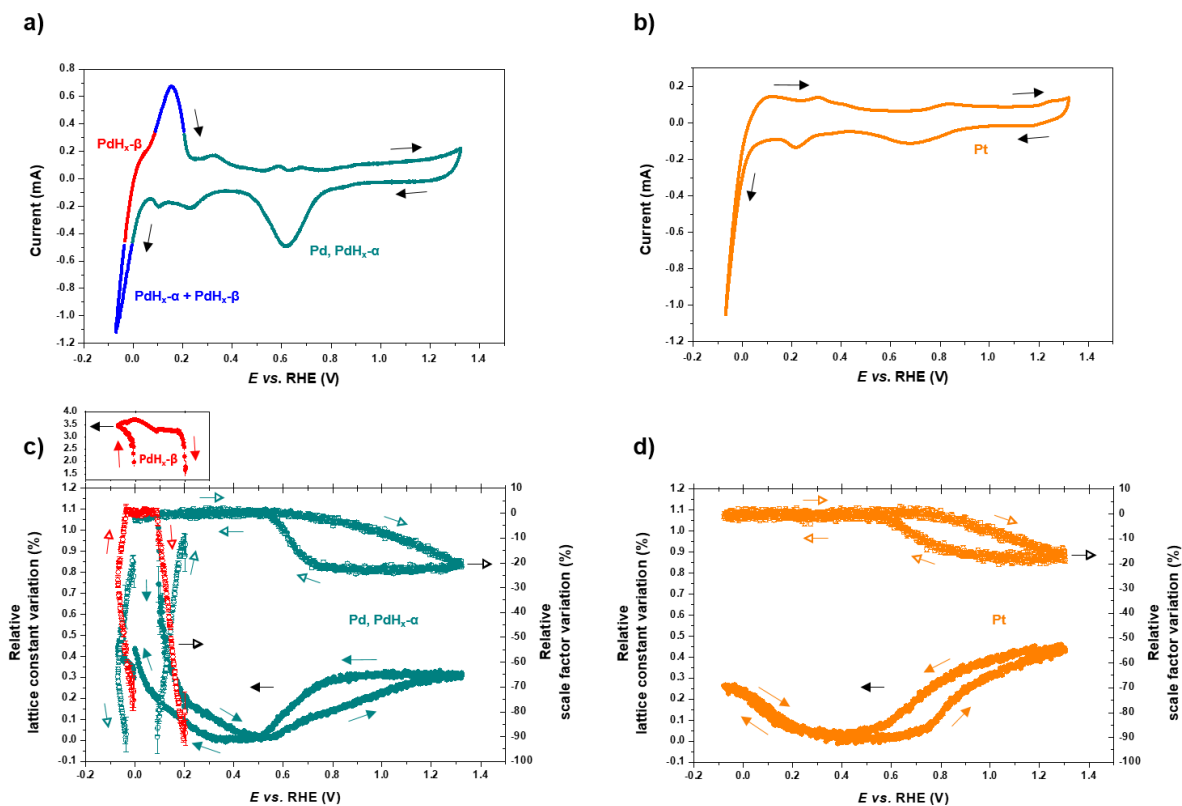
Figure 2: High time resolution monitoring of nanocatalysts microstructures during cyclic voltammetry. Cyclic voltammogram of the (a) Pd/C and (b) Pt/C catalysts in N₂-purged 0.1 M NaOH recorded at room temperature with a potential sweep rate of 5 mV s⁻¹; potential-dependency of the relative lattice constant variation (filled symbols, left axis) and relative scale factor (Bragg peaks area) variation (hollow symbols, right axis for the (c) Pd/C and (d) Pt/C catalysts. In a), the recorded electrical current is colored in cyan when only the phase Pd or PdH_x-α is detected, in red when only the PdH_x-β is detected and in blue when both PdH_x-α and PdH_x-β are detected simultaneously. In c) the signals colored in cyan correspond to the Pd or PdH_x-α

phase and the signals colored in red correspond to the PdH$_x$-β phase. For the sake of clarity, the relative lattice constant variation of PdH$_x$-β phase is represented in a separated plot with linked x-axis. The reference lattice constant values are 3.8890 Å and 3.9085 Å for Pd and Pt, respectively. In all panels, the signals are displayed as scatter points (333 ms time resolution) and the error bars represent the standard deviation associated with the refinement of the plotted parameters. The electrodes were loaded with 1.45 $mg_{metal} cm^{-2}$ an*d measured in transmission configuration.*

Transient core-shell mechanism of PdH$_x$ phase transition involving supersaturated and undersaturated hydrogenated phases.

The observed Pd lattice hysteresis during cyclic voltammetry experiment in **Figure 2.c** likely originates from combined thermodynamically-irreversible processes [13] and slow kinetics. We strive to disentangle these two aspects by showing Pd nanoparticles structural evolution during potential steps experiment. Various intermediate quasi-steady states are captured by consecutive 60 s potential holds along ascending and descending potential steps (staircase) of 100 mV (**Figure 3.a**). This potential hold duration should exceed the overall longest transition time (35 s for the complete absorption) measured in a control experiment (**Figure S2**). The as-obtained hysteresis plot (square symbols interpolated by black line and for $E \leq 0.40$ V *vs.* RHE) recalls the apparent violation of the Gibbs phase rule observed in the classical hydrogen pressure-composition isotherm for the Pd-H system in the gas phase [14]. In agreement with these former results, hydride formation appears thermodynamically-disfavored, with here a value of at least 100 mV overpotential compared to hydrogen desorption. Corresponding hydrogen content (H:Pd ratio) in the PdH$_x$-β phase can be estimated from the measured lattice constant and the calibration reported by Benck et al. [19], and the values are indicated in **Figure 3.a** as top axis. Note the maximum H:Pd ratio of 0.65 on Pd nanoparticles obtained in these experimental conditions at a potential of -200 mV *vs.* RHE would require H$_2$ pressure in the order of 100 MPa in the gas phase at room temperature [19,26]. In a dedicated study, Benck *et al*. could reach a H:Pd ratio as high as 0.96 on Pd thin film in 0.05 M H$_2$SO$_4$ electrolyte at -1.5 V *vs*. RHE [19].

Superimposing the points recorded during cyclic voltammetry (circles) on the quasi-steady state plot (**Figure 3.a**) reveals two significant features. The first is a striking, previously unreported, continuous dynamics for both PdH$_x$-α and PdH$_x$-β lattices observed during the PdH$_x$ $\alpha \leftrightarrow \beta$ transitions. This challenges the commonly accepted concept of constant α_{max} and β_{min} (maximum/minimum insertion contents in the PdH$_x$-α and PdH$_x$-β phases, respectively) during phase transition. In fact, the positions of both sets of reflections from XRD were reported invariant during the two-phase transition regime by Eastman et al. [17] (α_{max} of 3.9079 ± 0.002 Å and β_{min} of 4.0167 ± 0.002 Å in the gas phase at room temperature), in total contradiction with the present observations captured with high time resolution. One must note that very similar conclusions to Eastman's could have been reached here from the lower time resolution dataset obtained at the quasi-steady state in **Figure 3.a**, which shows an apparent α_{max} of 3.9033 ± 0.0006 Å and β_{min} of 4.0154 ± 0.002 Å. **Figure S3** shows selected WAXS patterns and associated Rietveld fits capturing the [220] reflections angular shifts for both phases during phase-transition. Our results support Lacher's idea introduced in 1937 [15,27] proposing the possibility of metastable supersaturation of the PdH$_x$-α phase and undersaturation of the PdH$_x$-β phase during the transitions. According to the Schwarz and Khachaturyan theory [16,28] now generally accepted to account for the Pd-H system hysteresis, this transient phenomenon is caused by the misfit-generated strain at the interface of the two phases with pronounced lattice mismatch. Our microstrain data, *i.e.* the local variations of the lattice constant within the individual phases, shown in **Figure S4** suggest this misfit-generated strain is mostly accommodated by the PdH$_x$-β phase. The second noticeable feature concerns the ~100 mV positive overpotential difference of the PdH$_x$ $\beta \rightarrow \alpha$ phase transition between steady state and cyclic voltammetry. This can be rationalized by slow hydrogen desorption kinetics that was reported to be dependent on both nanoparticle facets [20] and alkali metal cation [29].

More insights into the phase transition mechanism can be provided by Rietveld refinement. **Figure 3.b** shows an interesting evolution of the coherent domains sizes for the two phases: whereas the PdH$_x$-α domain size follows an expected full range size decrease (increase) during PdH$_x$ $\alpha \rightarrow \beta$ (PdH$_x$ $\beta \rightarrow \alpha$)

phase transition, the amplitude variation of the domain size for PdH_x-β is much narrower. This suggests that the core-shell evolution of the phase transitions observed in the gas phase for fine Pd nanoparticles (<10 nm) [18,30] is also valid in electrochemical environment. The PdH_x-β-shell thickening (possibly interpreted as a coherent hollow nanoparticle of decreasing inner void sizes) 'seen' as a solid particle of constant diameter by the Rietveld analysis of the WAXS pattern is supported by Burresi *et al*. recent work [31]. A slight increase of the PdH_x-β size and slight growth of the PdH_x-α size are observed during the early stage of PdH_x $\alpha \rightarrow \beta$ transition. An excess of the PdH_x-β size appears only during PdH_x $\beta \rightarrow \alpha$ transition. This perfectly illustrates the size-dependent transition kinetics of the nanoparticles composing the samples (see transmission electron microscopy images and associated particles size distributions, **Figure S5**). As smaller particles complete both transitions faster than large ones [30], the remaining volume-averaged size estimation provided by XRD at a given time produces the observed asymmetric trends. **Figure 3.b** illustrates the present findings regarding the PdH_x $\alpha \leftrightarrow \beta$ phase transition mechanism: the core-shell formation steps during absorption (panels (i) to (v)) are found reversible for desorption (panels (v) to (ix)).
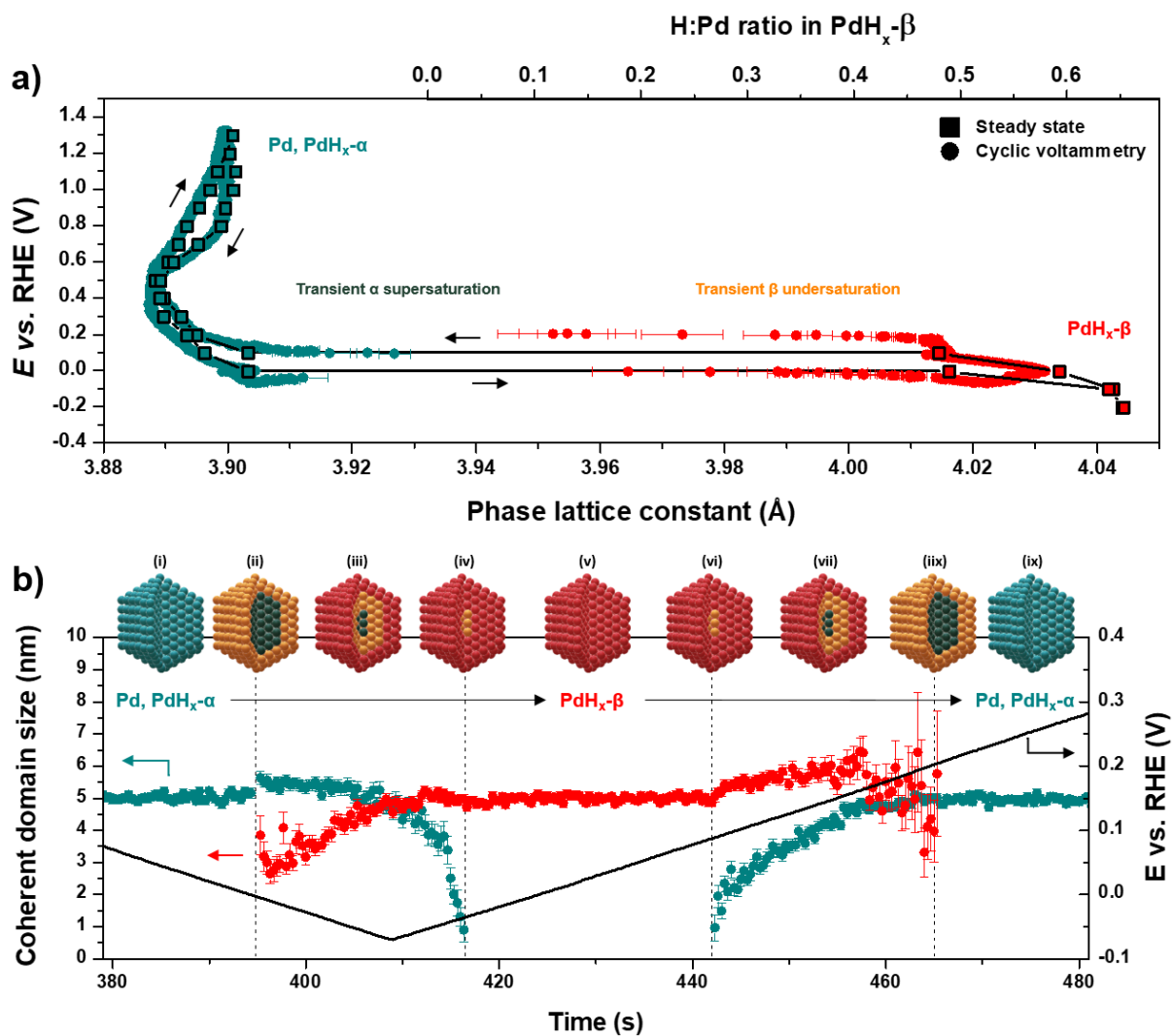
Figure 3: Monitoring hydrogen absorption on Pd nanocatalyst: *(a) PdH$_x$ α ↔ β phase transition lattice constants hysteresis at the steady state (square symbols interpolated by black lines) measured after 60 s hold at various potentials, superimposed with the data from cyclic voltammetry at 5 mV s^{-1} (circle symbols); b) evolution of coherent domain sizes as a function of time for the two phases transitions during cyclic voltammetry. In a), the H:Pd ratio in the PdH$_x$-β is deduced from the measured lattice parameter and the calibration trend from Ref [19]. In b) the deduced core-shell model evolution schematics for the phase transitions is presented, including the PdH$_x$- α (cyan), supersaturated PdH$_x$- α (dark cyan), undersaturated PdH$_x$- β (orange) and PdH$_x$- β (red) phases.*

**Electrochemical strain on Pt reveals its adsorption trends *operando***

It is well established from surface X-ray diffraction experiments on single crystals that, at fixed bulk properties, interplanar distances between the three first surface atomic layers are sensitive to adsorption processes [21–24]. Clearly, the enhanced surface-to-volume ratio of metal nanoparticles induces changes in the average lattice constant during adsorption processes that can be measured from simple powder X-ray diffraction experiments. **Figure 4.a** shows the cyclic voltammogram (solid line) and first derivative of the lattice parameter of an in-house Pt/C nanoparticles (dashed line) in typical electrocatalysis laboratory model conditions for proton-exchange membrane fuel cell studies (25 μg_{Pt} cm^{-2} thin-film in N$_2$-saturated 0.1 M HClO$_4$) recorded during *operando* WAXS. Compared to the commercial Pt/C catalyst from TKK, the synthesis route details of the in-house material are known and controlled (absence of surfactant, high purity precursors *etc*.). In addition, this in-house material features a narrower size distribution of 1.6 ± 0.3 nm compared to 2.1 ± 0.5 nm for TKK (see nanoparticle size distributions from transmission electron microscopy (TEM) images and synthesis route in the Supporting Information). Zeros of the lattice derivative reveal four local extrema on the electrochemical strain dynamics: two local lattice maxima located at the two potential limits (upper and lower, respectively) also with two local lattice minima almost superimposed at a value of 0.27 ± 0.01 V *vs*. RHE (see also orange curves in **Figure 4.b** and **4.c**). This potential value corresponds to the potential of zero total charge (pztc) measured by Chen *et al*. from CO displacement experiments on non-preferentially shaped Pt nanoparticles [32]. The authors reported pztc values of 0.26 V *vs*. RHE and 0.29 V *vs*. RHE in sulfuric and perchloric electrolytes, respectively. Our intermediate value is consistent with the presence of sulfonic acid groups from the perfluorosulfonic ionomer in our catalytic film (see Methods) even in perchloric acid electrolyte. This strongly suggests that the electrochemical strain is a direct consequence of charge adsorption processes on the surface of the nanoparticles: the lattice constant is minimum at the pztc and increases as adsorption of positively or negatively charged species proceeds (at electrode potential below or above the pztc, respectively).
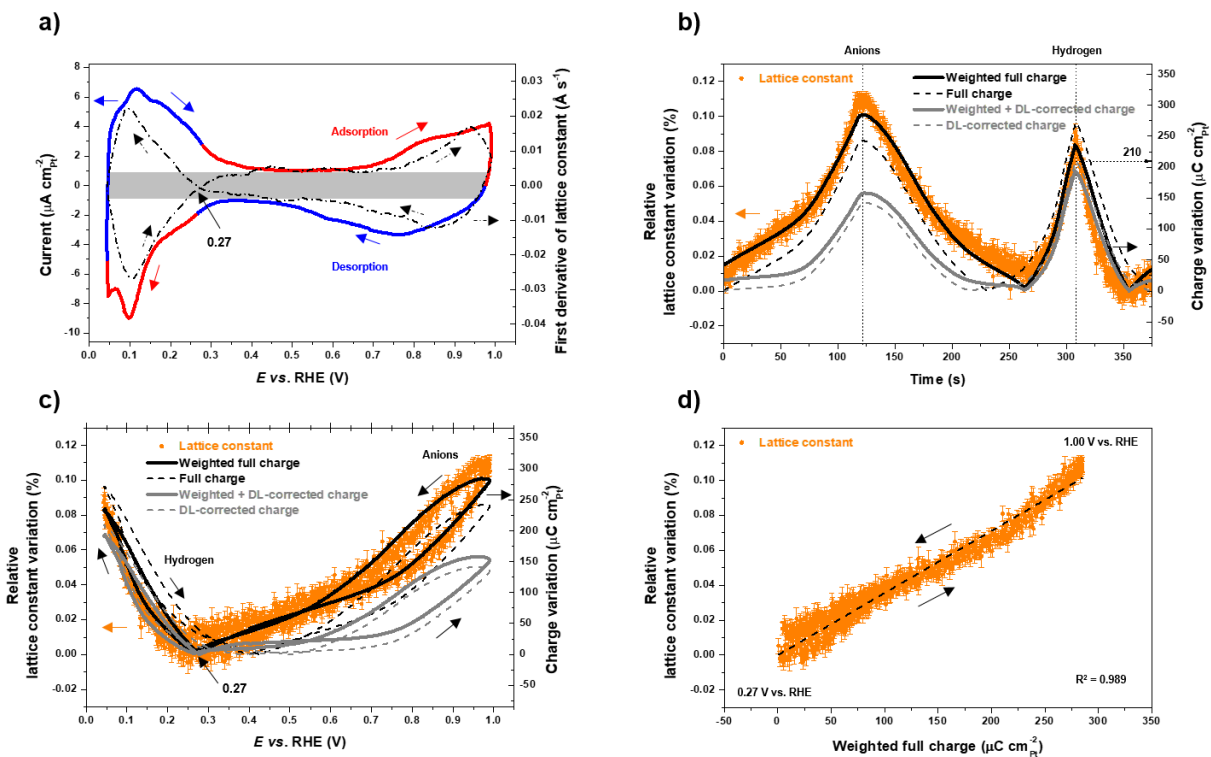
Figure 4: Monitoring adsorption on Pt: *(a) cyclic voltammograms (solid line) and first derivative of the lattice constant (dashed line) of Pt/C in N₂-purged 0.1 M HClO₄ recorded at room temperature with a potential sweep rate of 5 mV s⁻¹; associated relative lattice constant variation (orange) and electrical charge variation estimated from different electrical current integration methods (introducing weights for adsorbates and/or subtraction of the double layer current) as a function of (b) time and (c) electrode potential averaged along several potential cycles; (d) linear regression (dash line) between lattice constant variation and adsorbate-weighted full charge. In a) the grey box represents the estimation of the double layer on the cyclic voltammogram. The electrode was loaded with 25 μg_{Pt} cm^{-2} and the WAXS measured in grazing incidence configuration. The Pt surface area was estimated from the double-layer corrected hydrogen desorption current coulometry (without weight), assuming a conversion factor of 210 μC cm_{Pt}^{-2}.* ==*The reference lattice constant value of Pt is 3.9150 Å* ==*.The error bars represent the standard deviation associated with the refinement of the plotted parameters.*

To bridge the adsorbate surface coverage with the nanoparticles lattice constant variation, the electrical current passed through the electrode was integrated by possibly introducing a weight based on the sign of the first derivative of the lattice constant at a given potential: +1 when positive (corresponding to

adsorption, red regions on the cyclic voltammogram in **Figure 4.a**), and -1 when negative (corresponding to desorption, blue regions of the cyclic voltammogram in **Figure 4.a**). The current integration was also performed with and without prior subtraction of the double layer current (represented by the grey box in **Figure 4.a**). The superimposition of such integrated charges dataset with the relative lattice constant variation *versus* time or potential are shown in **Figure 4.b** and **Figure 4.c**, respectively. Depending on the hypothesis chosen for the integration, the direct correlation between adsorbate formation and nanoparticle lattice expansion is more or less established. Excluding the double layer current has an important impact on the charge variation amplitude ratio between hydrogen and anions regions, whereas the introduction of weights for adsorbates controls mostly the position of minimum charge. Clearly, the full adsorbate weighted charge agrees better with the lattice variations. In fact, such adsorption trends in the double layer region are in complete agreement with surface X-ray diffraction experiments [21–24] and especially electrochemical quartz-crystal micro- or nano- balances (EQCM, EQCN) experiments on single crystals. Using a method introduced by Uchida *et al.* [33] exploiting the linear correlation existing between Pt electrode mass variation and the measured charge transfer (including the double layer current), numerous studies [34–37] identified the adsorption of water, OH^-, ClO_4^- and HSO_4^- anions, or of the ionomer (if any) in both $HClO_4$ and H_2SO_4 electrolytes. Here, we show in **Figure 4.d** that a robust linear relationship also exists between the (relative) variation of the lattice constant and the measured charge transfer for both potential sweep directions from the pztc and 1.0 V *vs*. RHE. This discovery is of primary importance because it suggests the experimentally accessible lattice constant can be a structural descriptor of nanoparticles adsorption trends. Most importantly, contrary to the bulk electrode overall mass, this descriptor is an intrinsic property of the catalyst alone, which can be measured directly on practical nanocatalysts during operation, beyond any current experimental approaches [38]. Despite not explicitly provided from this method at this stage, information on the chemical nature of the adsorbates is likely encoded in the slope of the trend in **Figure 4.d**, which calls for a theoretical formalization of the reported phenomenon. Still, for adsorption, the surface electrical charge density is directly related to surface atoms average oxidation state, which gives information on possible adsorbates, as discussed below.
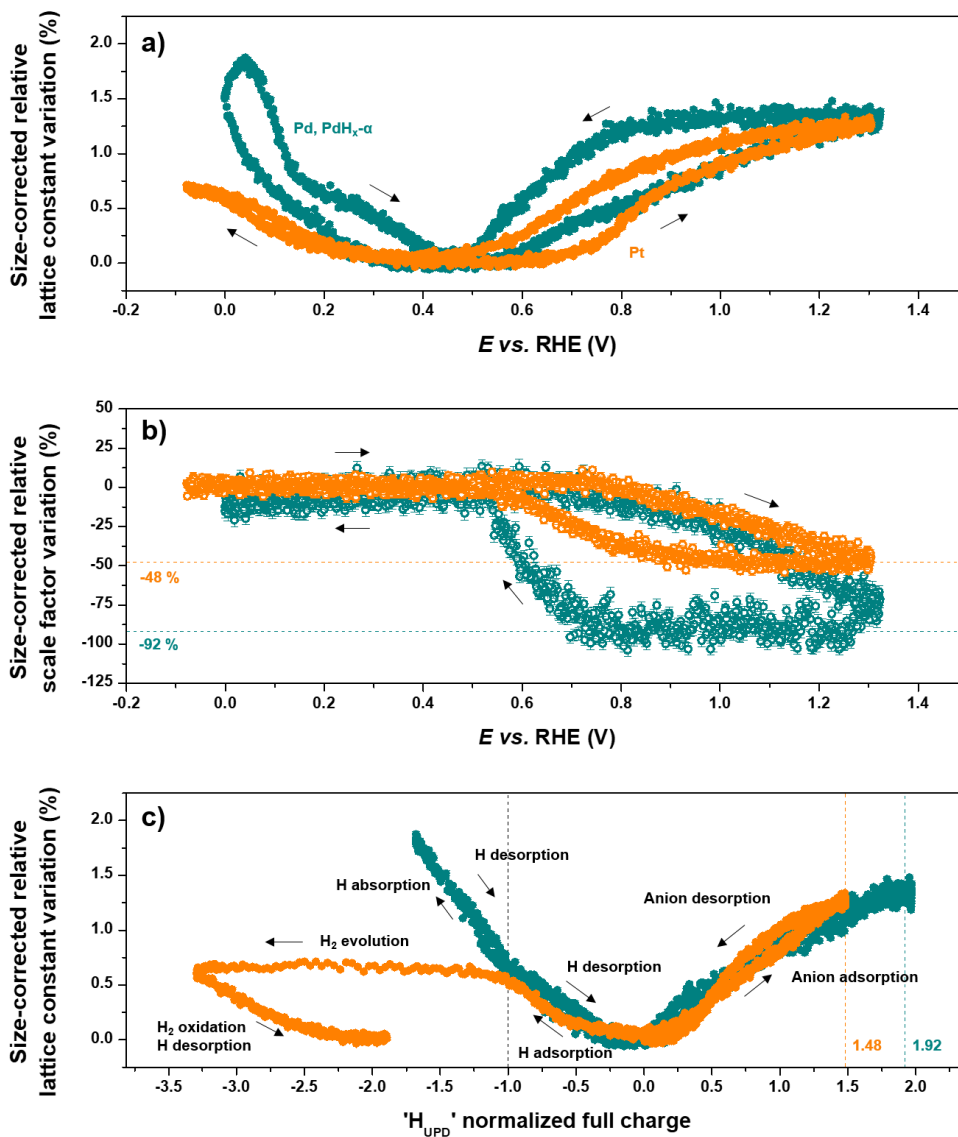
Figure 5: *Disentangling adsorption, absorption and Faradaic processes from their fingerprints on catalysts microstructure: (a) Size-corrected relative lattice constant variation and (b) size-corrected scale factor variation for Pd/C and Pt/C catalysts as a function of electrode potential; (c) size-corrected lattice constant variation as a function of 'H$_{UPD}$' normalized full charge during cyclic voltammetry in N$_2$-saturated 0.1 M NaOH. In c) the 'H$_{UPD}$' is estimated from the electrical charge passed at the slope break in the lattice trends. The reference lattice constant values are 3.8890 Å and 3.9085 Å for Pd and Pt, respectively. The signals are displayed as scatter points (333 ms time resolution) and the error bars represent the standard deviation associated with the refinement of the plotted parameters. The electrodes were loaded with 1.45 mg_{metal} cm^{-2} and measured in transmission configuration.*

Fingerprints of absorption, adsorption and Faradaic processes on electrochemical strain

The present results make clear that both absorption and adsorption processes contribute to nanoparticles lattice expansion. Comparing trends on Pd and Pt in alkaline electrolyte **(Figure 5)** shows that these processes, together with Faradaic reactions (such as hydrogen evolution), can still be distinguished from each other. To clarify the comparison, however, the low potential vertex of the cyclic voltammetry in this dedicated experiment was up-shifted to 0.00 V *vs*. RHE for Pd to prevent the formation of the PdH$_x$-β phase (while hydrogen absorption still occurs in PdH$_x$-α). **Figure 5.a** and **5.b** show the relative, size-corrected evolutions of the lattice constants and scale factors, respectively, measured for the two materials during cyclic voltammetry. The proposed correction from the size consists of dividing the raw structural parameters values by the dispersion (the proportion of surface atoms, in %) and was found necessary when comparing two materials of different particle sizes [39,40] (correction details are provided in the Supporting Information). In light of the lattice constant changes, **Figure 5.a** makes clear that in the 0.60 ≤ E ≤ 0.90 V *vs*. RHE potential window and these experimental conditions, Pt features lower oxides surface coverage than Pd (despite the smaller size of the Pt nanoparticles versus Pd ones, **Figure S5**), which signs the larger oxophillicity of Pd versus Pt. The size-corrected, relative scale factor losses plotted in **Figure 5.b** can be directly interpreted as the fraction of the surface undergoing place exchange amorphisation (in %). The value at 1.32 V *vs*. RHE is found higher for Pd (-92%), which results in larger irreversibility during the negative-going potential scan compared to Pt (-48%). As previously discussed, different lattice constant evolutions between Pd and Pt are observed during electrode polarization below E = 0.40 V *vs*. RHE. Especially, from **Figure 5.a**, bulk hydrogen absorption is found to produce more pronounced lattice constant expansion than surface adsorption. Finally, **Figure 5.c** shows the variation of the lattice constants *versus* the 'H$_{UPD}$' normalized charge. Since the H$_{UPD}$ region is not defined on the cyclic voltammograms in these experimental conditions (H$_2$ evolution/oxidation on Pt and bulk absorption/desorption on Pd), the values were estimated from the electrical charge passed at the slope break in the lattice constant variation between hydrogen adsorption and either hydrogen evolution on Pt

or hydrogen absorption on Pd. These slope breaks consequently appear at the -1 vertical line in **Figure 5.c**. Below this limit, Pt catalyzes the hydrogen evolution with constant lattice expansion, whereas Pd undergoes hydrogen absorption. The viability of the approach consisting of disentangling hydrogen adsorption from absorption and evolution from their impact on the lattice constant evolution trends is shown by its consistent impact on the oxidation trends. In fact, such H_{UPD} estimation leads to a charge ratio at maximum oxidation very close to 1.48 for Pt and 1.92 for Pd (see dashed-lines). Attributing these charges to Pt and Pd translates into O_{ads} (2-electron process) surface coverages of 0.48 and 0.92 for Pt and Pd (if the rest of the surface is covered by 1-electron process OH_{ads}), respectively. These values are the ones found from the O_{ads} induced [41] place-exchange amorphisation revealed by the size-corrected relative scale factor losses in **Figure 5.b**. These convergent observations strongly support the proposed disentanglement of the different electrochemical processes based on the feedback of their distinct fingerprints on catalysts microstructures, as labeled in **Figure 5.c**.

Atomistic description of electrochemical strain and its implication in electrocatalysis

Surface strain in nanocatalysts has so important consequences on their catalytic properties, that 'strain-engineering' has emerged as a fruitful approach toward the design of more active materials for a wide range of applications [42–44]. In that context, more than a convenient characterization tool allowing probing nanocatalysts adsorption trends *operando*, the presented electrochemical strain may at least partially control the revealed adsorption trends. Consequently, how much the systematic structural changes dynamics observed here are predicted to affect the electrocatalytic properties is a fundamental question.

We take the oxygen reduction reaction (ORR) as an example reaction using our dataset on Pt/C thin-film catalyst measured in model 0.1 M $HClO_4$ conditions and presented in **Figure 4**. The influence of Pt surface strain on its ORR performance is largely documented [42–44], and implementing moderate compressive strain is shown desirable to maximize the ORR activity by optimizing hydroxyl groups

adsorption strength. The tensile strain observed here during adsorption, however, should favor site poisoning and be detrimental to the ORR (excepted some specific reported cases [42]). As shown in **Figure 4.b-d**, the measured *global* tensile strain does not exceed 0.12 % in the range $0.05 \leq E \leq 1.0$ V *vs*. RHE *relatively* to the structure of Pt at the pztc. Rationalizing this strain amplitude value in the frame of the ORR electrocatalysis, however, requires discussing the *surface* and *absolute* strain (or at least compared to a model reference state). The near-constant microstrain values (representative of lattice constant heterogeneity) measured during cyclic voltammetry experiment displayed in **Figure 6.a** provide fundamental insights on the atomistic origin of the electrochemical strain: the latter is varying homogeneously in the nanoparticle. Consequently, the observed changes in the lattice can be attributed to the whole nanoparticle without distinction of the surface from the bulk. Note the near-constant but positive values of microstrain recorded indicate 'native' local heterogeneities exist in the lattice (defects such as grain boundaries [39], stress round steps, edges or from nanoparticle-support interactions [45] *etc*.). Interestingly, the slight microstrain decrease observed in the H_{UPD} potential region attests of very good sensitivity of this parameter, since hydrogen adsorption is known to produce reversible step-edges roughening of Pt surfaces during such cyclic voltammetry experiments [46]. The ability of nanoparticles to accommodate the surface adsorbate-induced strain with the complete bulk is a first distinction compared to single crystals. As shown in **Figure 6.b**, the *in situ* surface XRD data from Kondo *et al*. [22] (blue curves), recorded in similar conditions of this study show a strong tensile unilateral strain gradient between the two first interplanar distances of Pt(111) single crystal (d_{12} and d_{23}, for first and second, respectively) during hydrogen adsorption. Note the third interatomic distance was found not modified compared with the bulk. The second distinctive feature concerns the potential region of interest for the ORR: whereas the adsorption of hydroxyl groups is found to be completely relax Pt(111) surface between $0.75 \leq E \leq 0.9$ V *vs*. RHE, this is where the strain dynamics in nanoparticles is the more pronounced (see **Figure 4.b-c**). Since this strain can be attributed to the surface (and bulk) of the nanoparticles, its impact on ORR can be estimated. **Figure 6.b** displays a non-exhaustive literature data overview of the strain in different pure Pt surface systems: the above discussed *operando* Pt(111) single

crystal data from Kondo *et al*. (blue curves), the *ex situ* data on Pt_xCu_{100-x} core-shell catalysts from Strasser *et al*. [43] (red lines), and the *operando* data on Pt nanoparticles investigated in this study (orange curve). The strain values are represented in absolute scale *via* the d_{111} interplanar distances (left axis) and their associated values relative to the reference bulk Pt (right axis). As expected for nanoparticles due to their higher surface energy [47], the plot first shows the Pt/C catalyst exhibits a slight compressive strain (negative values) over the whole potential range investigated. As schematized in **Figure 6.c**, the compressed nanoparticles oscillate between the influences of surface tension and adsorbates, the latter may partially attenuate the former. But most of all, the comparative plot in **Figure 6.b** makes clear the insignificance of the electrochemical strain variation amplitude (between *c.a.* -0.13% and -0.22 % in the landscape of strain-engineered nanocatalysts for the ORR. In fact, desirable nanocatalysts 'strained-by-design' features *ex-situ* compressive strain values on the pure Pt surface one order of magnitude higher (see Pt_xCu_{100-x} core-shell catalysts). Especially, the density functional theory (DFT) calculations from previous contributions [43,48] plotted in **Figure 6.d** predict the optimal strain value of *c.a.* -1.75% to be implemented in surface Pt for maximized ORR performance (without contribution from other effects). The non-conventional representation of this DFT trend with linear ORR activity axis helps realizing that, however, the impact of only 0.1 % overall compressive strain loss due to the electrochemical tensile strain contribution at $E=$ 0.90 V *vs*. RHE would not produce the same effect on ORR activity depending on the catalyst initial position on the curve. In the case of the present pure Pt nanoparticles, this constitutes only a 0.26-fold difference in activity, whereas a catalyst *a priori* located at the apex of the curve would lose 3.5 unit of enhancement factor. Besides, quantification of electrochemical tensile strain on more advanced 'strained-by-design' and/or shape-controlled multimetallic materials is still to be performed.
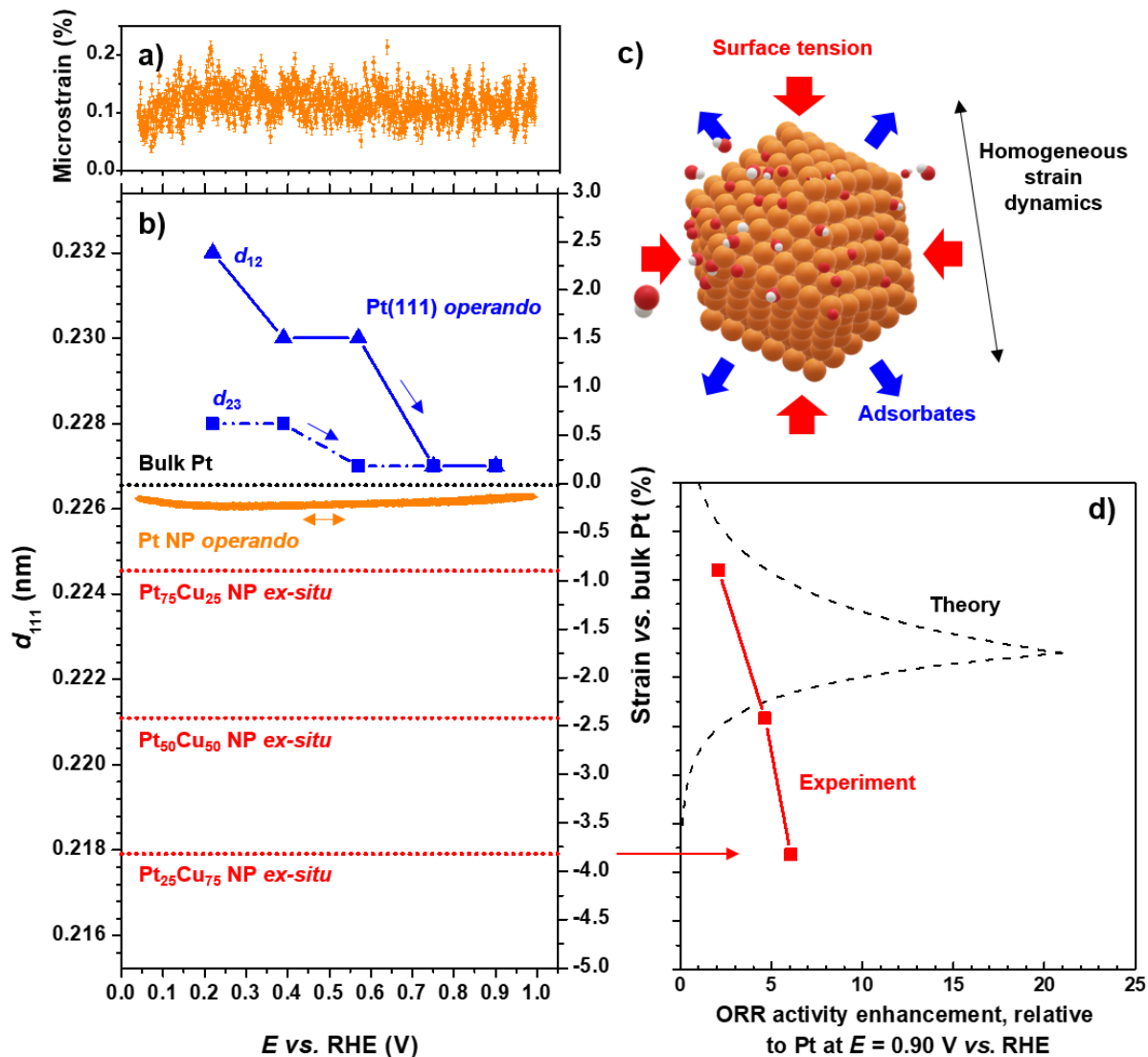
Figure 6: Electrochemical strain in the ORR electrocatalysis landscape*: (a) Microstrain values measured during cyclic voltammetry experiment of Pt/C catalyst plotted as a function of the electrode potential; (b) strain vs. electrode potential operando data for Pt(111) single crystal from Kondo et al. surface XRD measurements adapted from Ref[22] (blue curves) and Pt/C catalyst from this study (orange curve), strain in the Pt shell of a family of Pt_xCu_{100-x} core-shell catalysts measured ex situ from anomalous XRD adapted from Ref[43]; (c) schematic showing the two opposite effects of surface tension and adsorbates formation on establishing the strain dynamics of a Pt nanoparticle in ORR environment; (d) experimental ORR activity as a function of compressive strain for the family of Pt_xCu_{100-x} core-shell catalysts of panel b) with theoretical trend estimated from DFT calculations in Ref[43] and further adapted by Ref[48]. In panel b) d_{12} and d_{23} are the first and second*

CONCLUSIONS

In summary, we used the brilliance of the 4th generation ESRF-EBS light source to investigate the structures of device-relevant Pd and Pt nanocatalysts during cyclic voltammetry. Beyond the technical showcase of the new source, our study firstly reveals that the bulk microstructures (lattice constant, crystal phase or coherence) of such device-relevant catalysts with enhanced surface-to-volume ratio are permanently modified by the electrochemical environment relevant of their application systems (electrochemical adsorption and absorption of hydrogen and oxides species). Secondly, monitoring the structure of Pd/C during cyclic voltammetry and potential staircase allowed us to unveil the electrochemically-driven Pd hydrides phase transition, which was until now mostly investigated in the gas phase. The fine XRD patterns measured *operando* provided the first detection of theoretically predicted supersaturated and undersaturated metastable states, involved in a core-shell mechanism of the phase transition. Thirdly, monitoring the structure of Pt/C during cyclic voltammetry on electrode thin film in typical conditions of fuel cell electrocatalysis laboratory allowed establishing near-linear correlation between the bulk lattice of Pt nanoparticles and oxides surface coverage. Since the latter is known to be a descriptor of catalysts activity toward numerous reactions (oxygen reduction and fuel oxidation) and stability (oxidation and dissolution), the measurement of the lattice parameter according to our proposed approach allows experimental access to these descriptors in device-relevant sample environments *operando*. This constitutes a main advantage compared to spectroscopic techniques and is foreseen to find a wide range of applications. Fourthly, comparing trends observed on Pd/C and Pt/C shows that adsorption and absorption processes have distinct impacts on the bulk lattice constant expansion. Such fingerprints allow disentangling the two processes from each other in a general fashion. Finally, since the

21

electronic structure (*d*-band centre) of the catalytic sites is likely impacted by the observed strain dynamics, we provided a more precise atomistic description of this strain in the case of Pt in perchloric acid electrolyte. Notably, we showed the strain dynamics proceeds homogeneously in the nanoparticles, which means the surface strain is known in a potential resolved fashion. Taking the ORR as an exemplary reaction, and in light of previous reports, we showed the adsorbate-induced tensile strain must not significantly degrade the ORR performance in the case of pure Pt nanoparticles. However, this strain dynamics is currently overlooked by the theoretical models driving the catalyst-by-design approach of more advanced nanocatalysts, from which the trends in electrochemical strain remain unknown.

ASSOCIATED CONTENT

Supporting Information: Details and methods about the electrocatalysts used, electrochemical measurements, synchrotron wide-angle X-ray scattering measurements, Rietveld refinement and correction of microstructural data from nanoparticle size.

AUTHOR INFORMATION

Corresponding Author

Raphaël Chattot, European Synchrotron Radiation Facility, ID 31 Beamline, BP 220, F-38043 Grenoble, France; https://orcid.org/0000-0001-6169-530X; email: raphael.chattot@grenoble-inp.org

Authors

Isaac Martens, European Synchrotron Radiation Facility, ID 31 Beamline, BP 220, F-38043 Grenoble, France; orcid.org/0000-0001-8342-6629

Marta Mirolo, European Synchrotron Radiation Facility, ID 31 Beamline, BP 220, F-38043 Grenoble, France; orcid.org/0000-0002-6781-2762

Michal Ronovsky, European Synchrotron Radiation Facility, ID 31 Beamline, BP 220, F-38043 Grenoble, France

Florian Russello, European Synchrotron Radiation Facility, ID 31 Beamline, BP 220, F-38043 Grenoble, France

Helena Isern Herrera, European Synchrotron Radiation Facility, ID 31 Beamline, BP 220, F-38043 Grenoble, France

Guillaume Braesch, Univ. Grenoble Alpes, Univ. Savoie Mont Blanc, CNRS, Grenoble INP, LEPMI, 38000

Elisabeth Hornberger, Electrochemical Energy, Catalysis and Material Science Laboratory, Department of Chemistry, Technische Universität Berlin, 10623 Berlin, Germany; orcid.org/0000-0003-4548-8911

Peter Strasser, Electrochemical Energy, Catalysis and Material Science Laboratory, Department of Chemistry, Technische Universität Berlin, 10623 Berlin, Germany

Eric Sibert, Univ. Grenoble Alpes, Univ. Savoie Mont Blanc, CNRS, Grenoble INP, LEPMI, 38000; orcid.org/0000-0003-4084-1624

Marian Chatenet, Univ. Grenoble Alpes, Univ. Savoie Mont Blanc, CNRS, Grenoble INP, LEPMI, 38000 ; orcid.org/0000-0002-9673-4775

Veijo Honkimäki, European Synchrotron Radiation Facility, ID 31 Beamline, BP 220, F-38043 Grenoble, France ; orcid.org/0000-0001-7549-981X

Jakub Drnec, European Synchrotron Radiation Facility, ID 31 Beamline, BP 220, F-38043 Grenoble, France ; orcid.org/0000-0002-9520-1555
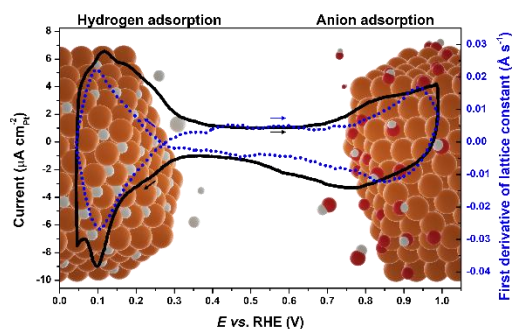
ACKNOWLEDGEMENTS

REFERENCES

(1)   Henry, C. R. Surface Studies of Supported Model Catalysts. *Surf. Sci. Rep.* **1998**, *31*, 231–325.

(2)   Markovic, N. M.; Ross Jr., P. N. Surface Science Studies of Model Fuel Cell Electrocatalysts. *Surf. Sci. Rep.* **2002**, *45* (4–6), 117–229.

(3)   Nørskov, J. K.; Rossmeisl, J.; Logadottir, a.; Lindqvist, L.; Kitchin, J. R.; Bligaard, T.; Jónsson, H. Origin of the Overpotential for Oxygen Reduction at a Fuel-Cell Cathode. *J. Phys. Chem. B* **2004**, *108* (46), 17886–17892.

(4)   Jiao, Y.; Zheng, Y.; Jaroniec, M.; Qiao, S. Z. Design of Electrocatalysts for Oxygen- and Hydrogen-Involving Energy Conversion Reactions. *Chem. Soc. Rev.* **2015**, *44* (8), 2060–2086.

(5)   Nørskov, J. K.; Bligaard, T.; Rossmeisl, J.; Christensen, C. H. Towards the Computational Design of Solid Catalysts. *Nat. Chem.* **2009**, *1* (1), 37–46.

(6)   Hammes-Schiffer, S. Catalysts by Design: The Power of Theory. *Acc. Chem. Res.* **2017**, *50* (3), 561–566.

(7)   Zhao, Z.; Liu, S.; Zha, S.; Cheng, D.; Studt, F.; Henkelman, G.; Gong, J. Theory-Guided Design of Catalytic Materials Using Scaling Relationships and Reactivity Descriptors. *Nat. Rev. Mater.* **2019**, *4*, 792–804.

(8)   Mistry, H.; Varela, A. S.; Kühl, S.; Strasser, P.; Cuenya, B. R. Nanostructured Electrocatalysts with Tunable Activity and Selectivity. *Nat. Rev. Mater.* **2016**, *1* (4), 16009.

(9)   Calle-Vallejo, F.; Koper, M. T. M.; Bandarenka, A. S. Tailoring the Catalytic Activity of Electrodes with Monolayer Amounts of Foreign Metals. *Chem. Soc. Rev.* **2013**, *42* (12), 5210–5230.

(10)   Cherevko, S.; Zeradjanin, A. R.; Topalov, A. A.; Kulyk, N.; Katsounaros, I.; Mayrhofer, K. J. J. Dissolution of Noble Metals during Oxygen Evolution in Acidic Media. *ChemCatChem* **2014**, *6* (8), 2219–2223.

(11)   Lafforgue, C.; Zadick, A.; Dubau, L.; Maillard, F.; Chatenet, M. Selected Review of the Degradation of Pt and Pd-Based Carbon-Supported Electrocatalysts for Alkaline Fuel Cells: Towards Mechanisms of Degradation. *Fuel Cells* **2018**, *18* (3), 229–238.

(12)   You, H.; Nagy, Z.; Zurawski, D. J.; Chiarello, R. P. Place-Exchange Mechanism of Pt(111) Oxidation/Reduction as Observed by Synchrotron X-Ray Scattering. *Proc. 6th Int. Symp. Electrode Process.* **2008**, *23* (5), 7–9.

(13) Lewis, F. A. The Hydrides of Palladium and Palladium Alloys. *Platin. Met. Rev.* **1960**, *4* (4), 132–137.

(14) Lewis, F. A. The Palladium-Hydrogen System: Structures near Phase Transition and Critical Points. *Int. J. Hydrogen Energy* **1995**, *20* (7), 587–592.

(15) Scholtus, N. A.; Keith Hall, W. Hysteresis in the Palladium-Hydrogen System. *J. Chem. Phys.* **1962**, *39* (4), 868–870.

(16) Schwarz, R. B.; Khachaturyan, A. G. Thermodynamics of Open Two-Phase Systems with Coherent Interfaces: Application to Metal-Hydrogen Systems. *Acta Mater.* **2006**, *54* (2), 313–323.

(17) Eastman, J. A.; Thompson, L. J.; Kestel, B. J. Narrowing of the Palladium-Hydrogen Miscibility Gap in Nanocrystalline Palladium. *Phys. Rev. B* **1993**, *48* (1), 84–93.

(18) Bugaev, A. L.; Guda, A. A.; Lomachenko, K. A.; Shapovalov, V. V.; Lazzarini, A.; Vitillo, J. G.; Bugaev, L. A.; Groppo, E.; Pellegrini, R.; Soldatov, A. V.; et al. Core-Shell Structure of Palladium Hydride Nanoparticles Revealed by Combined X-Ray Absorption Spectroscopy and X-Ray Diffraction. *J. Phys. Chem. C* **2017**, *121* (33), 18202–18213.

(19) Benck, J. D.; Jackson, A.; Young, D.; Rettenwander, D.; Chiang, Y. M. Producing High Concentrations of Hydrogen in Palladium via Electrochemical Insertion from Aqueous and Solid Electrolytes. *Chem. Mater.* **2019**, *31* (11), 4234–4245.

(20) Johnson, N. J. J.; Lam, B.; MacLeod, B. P.; Sherbo, R. S.; Moreno-Gonzalez, M.; Fork, D. K.; Berlinguette, C. P. Facets and Vertices Regulate Hydrogen Uptake and Release in Palladium Nanocrystals. *Nat. Mater.* **2019**, *18* (5), 454–458.

(21) Nakamura, M.; Nakajima, Y.; Hoshi, N.; Tajiri, H.; Sakata, O. Effect of Non-Specifically Adsorbed Ions on the Surface Oxidation of Pt(111). *ChemPhysChem* **2013**, *14* (11), 2426–2431.

(22) Kondo, T.; Masuda, T.; Aoki, N.; Uosaki, K. Potential-Dependent Structures and Potential-Induced Structure Changes at Pt(111) Single-Crystal Electrode/Sulfuric and Perchloric Acid Interfaces in the Potential Region between Hydrogen Underpotential Deposition and Surface Oxide Formation by in Situ Su. *J. Phys. Chem. C* **2016**, *120* (29), 16118–16131.

(23) Liu, Y.; Kawaguchi, T.; Pierce, M. S.; Komanicky, V.; You, H. Layering and Ordering in Electrochemical Double Layers. *J. Phys. Chem. Lett.* **2018**, *9* (6), 1265–1271.

(24) Liu, Y.; Barbour, A.; Komanicky, V.; You, H. X-Ray Crystal Truncation Rod Studies of Surface Oxidation and Reduction on Pt(111). *J. Phys. Chem. C* **2016**, *120* (29), 16174–16178.

(25) Martens, I.; Chattot, R.; Rasola, M.; Blanco, M. V. M. V.; Honkimäki, V.; Bizzotto, D.; Wilkinson, D. P. D. P.; Drnec, J. Probing the Dynamics of Platinum Surface Oxides in Fuel Cell Catalyst Layers Using in Situ X-Ray Diffraction. *ACS Appl. Energy Mater.* **2019**, *2* (11), 7772–7780.

(26) Yamauchi, M.; Kobayashi, H.; Kitagawa, H. Hydrogen Storage Mediated by Pd and Pt Nanoparticles. *ChemPhysChem* **2009**, *10* (15), 2566–2576.

(27) Lacher, J. R. A Theoretical Formula for the Solubility of Hydrogen in Palladium. *Proc. R. Soc.*

London. Ser. A **1937**, *161* (907), 525–545.

(28)   Schwarz, R. B.; Khachaturyan, A. G. Thermodynamics of Open Two-Phase Systems with Coherent Interfaces. *Phys. Rev. Lett.* **1995**, *74* (13), 2523–2526.

(29)   Czerwinski, A.; Marassi, R. The Absorption of Hydrogen and Deuterium in Thin Palladium Electrodes. Part II: Basic Solutions. *J. Electroanal. Chem.* **1992**, *322* (1–2), 373–381.

(30)   Langhammer, C.; Zhdanov, V. P.; Zorić, I.; Kasemo, B. Size-Dependent Kinetics of Hydriding and Dehydriding of Pd Nanoparticles. *Phys. Rev. Lett.* **2010**, *104* (13), 2–5.

(31)   Burresi, E.; Tapfer, L. Diffraction Line Profiles of Spherical Hollow Nanocrystals. *Nanomater. Nanotechnol.* **2019**, *9*, 1–11.

(32)   Chen, Q. S.; Solla-Gullón, J.; Sun, S. G.; Feliu, J. M. The Potential of Zero Total Charge of Pt Nanoparticles and Polycrystalline Electrodes with Different Surface Structure: The Role of Anion Adsorption in Fundamental Electrocatalysis. *Electrochim. Acta* **2010**, *55* (27), 7982–7994.

(33)   Uchida, H.; Ikeda, N.; Watanabe, M. Electrochemical Quartz Crystal Microbalance Study of Copper Adatoms on Gold Electrodes Part II. Further Discussion on the Specific Adsorption of Anions from Solutions of Perchloric and Sulfuric Acid. *J. Electroanal. Chem.* **1997**, *424* (1–2), 5–12.

(34)   Gloaguen, F.; Léger, J. M.; Lamy, C. Electrochemical Quartz Crystal Microbalance Study of the Hydrogen Underpotential Deposition at a Pt Electrode. *J. Electroanal. Chem.* **1999**, *467* (1), 186–192.

(35)   Santos, M. C.; Miwa, D. W.; Machado, S. A. S. Study of Anion Adsorption on Polycrystalline Pt by Electrochemical Quartz Crystal Microbalance. *Electrochem. commun.* **2000**, *2* (10), 692–696.

(36)   Jerkiewicz, G.; Vatankhah, G.; Lessard, J.; Soriaga, M. P.; Park, Y. S. Surface-Oxide Growth at Platinum Electrodes in Aqueous H2SO 4 Reexamination of Its Mechanism through Combined Cyclic-Voltammetry, Electrochemical Quartz-Crystal Nanobalance, and Auger Electron Spectroscopy Measurements. *Electrochim. Acta* **2004**, *49* (9–10), 1451–1459.

(37)   Garrick, T. R.; Moylan, T. E.; Yarlagadda, V.; Kongkanand, A. Characterizing Electrolyte and Platinum Interface in PEM Fuel Cells Using CO Displacement. *J. Electrochem. Soc.* **2017**, *164* (2), F60–F64.

(38)   Bergmann, A.; Roldan Cuenya, B. Operando Insights into Nanoparticle Transformations during Catalysis. *ACS Catal.* **2019**, *9* (11), 10020–10043.

(39)   Chattot, R.; Asset, T.; Bordet, P.; Drnec, J.; Dubau, L.; Maillard, F. Beyond Strain and Ligand Effects: Microstrain-Induced Enhancement of the Oxygen Reduction Reaction Kinetics on Various PtNi/C Nanostructures. *ACS Catal.* **2017**, *7*, 398–408.

(40)   Chattot, R.; Bacq, O. Le; Beermann, V.; Kühl, S.; Herranz, J.; Henning, S.; Kühn, L.; Asset, T.; Guétaz, L.; Renou, G.; et al. Surface Distortion as a Unifying Concept and Descriptor in Oxygen Reduction Reaction Electrocatalysis. *Nat. Mater.* **2018**, *17* (9), 827–833.

(41)   Fuchs, T.; Drnec, J.; Calle-Vallejo, F.; Stubb, N.; Sandbeck, D. J. S.; Ruge, M.; Cherevko, S.;

Harrington, D. A.; Magnussen, O. M. Structure Dependency of the Atomic-Scale Mechanisms of Platinum Electro-Oxidation and Dissolution. *Nat. Catal.* **2020**, *3* (9), 754–761.

(42)   Luo, M.; Guo, S. Strain-Controlled Electrocatalysis on Multimetallic Nanomaterials. *Nat. Rev. Mater.* **2017**, *2*, 1–14.

(43)   Strasser, P.; Koh, S.; Anniyev, T.; Greeley, J.; More, K.; Yu, C.; Liu, Z.; Kaya, S.; Nordlund, D.; Ogasawara, H.; et al. Lattice-Strain Control of the Activity in Dealloyed Core-Shell Fuel Cell Catalysts. *Nat. Chem.* **2010**, *2* (6), 454–460.

(44)   Xia, Z.; Guo, S. Strain Engineering of Metal-Based Nanomaterials for Energy Electrocatalysis. *Chem. Soc. Rev.* **2019**.

(45)   Daio, T.; Staykov, A.; Guo, L.; Liu, J.; Tanaka, M.; Matthew Lyth, S.; Sasaki, K. Lattice Strain Mapping of Platinum Nanoparticles on Carbon and SnO2 Supports. *Sci. Rep.* **2015**, *5*, 1–10.

(46)   McCrum, I. T.; Bondue, C. J.; Koper, M. T. M. Hydrogen-Induced Step-Edge Roughening of Platinum Electrode Surfaces. *J. Phys. Chem. Lett.* **2019**, *10* (21), 6842–6849.

(47)   Medasani, B.; Vasiliev, I. Computational Study of the Surface Properties of Aluminum Nanoparticles. *Surf. Sci.* **2009**, *603* (13), 2042–2046.

(48)   Stephens, I. E. L.; Bondarenko, A. S.; Grønbjerg, U.; Rossmeisl, J.; Chorkendorff, I. Understanding the Electrocatalysis of Oxygen Reduction on Platinum and Its Alloys. *Energy Environ. Sci.* **2012**, *5* (5), 6744–6762.

TABLE OF CONTENTS/ABSTRACT GRAPHICS

For Table of Contents Only